Inorganic Chemistry
Article

Inorg. Chem. **2010**, *49*, 8495–8503 **8495**
DOI: 10.1021/ic1011204

Iron Thiobiurets: Single-Source Precursors for Iron Sulfide Thin Films

Karthik Ramasamy, Mohammad A. Malik, Madeline Helliwell, Floriana Tuna, and Paul O'Brien*

The School of Chemistry and Manchester Materials Center, The University of Manchester,
Oxford Road, Manchester, M13 9PL U.K.

Received June 3, 2010

The iron(III) complexes of several 1,1,5,5-tetraalkyl-2-thiobiurets [Fe(SON(CN^{i}Pr$_2$)$_2$)$_3$ (**1**), Fe$_2$(μ-OMe)$_2$(SON(CNEt$_2$)$_2$)$_2$ (**2**), Fe(SON(CNEt$_2$)$_2$)$_3$ (**3**), and Fe(SON(CNMe$_2$)$_2$)$_3$ (**4**)] have been synthesized, and the single-crystal X-ray structures of **1**, **2**, and **4** have been determined. The magnetic properties of complex **2** as a function of the temperature and field were studied. Thermogravimetric analysis of complexes **1**−**4** showed the decomposition in one major step to iron sulfide residues. All four complexes were used as single-source precursors for the deposition of iron sulfide thin films by aerosol-assisted chemical vapor deposition. Complex **1** gave hexagonal troilite FeS films with a small amount of tetragonal pyrrhotites Fe$_{1-x}$S at 300 °C, whereas only troilite FeS was deposited at 350, 400, or 450 °C. Complexes **2** and **3** deposited a mixture of hexagonal troilite FeS and cubic pyrite FeS$_2$ films at all temperatures. Complex **4** deposited very thin films of FeS at all temperatures as troilite. Scanning electron microscopy images of the films deposited from all complexes showed that the morphology consisted of plates, granules, rods, and sheets like crystallites. The size and shapes of these crystallites were dependent on the growth temperature and the precursor used. This is the first time that iron(III) thiobiuret complexes have been used as single-source precursors for iron sulfide thin films.

Introduction

Iron sulfides are an interesting class of materials with many different forms, which include pyrite (cubic-FeS$_2$), marcasite (calcium chloride structure-FeS$_2$), troilite (FeS), mackinawite (Fe$_{1+x}$S), pyrrhotite (Fe$_{1-x}$S, Fe$_7$S$_8$), smythite (hexagonal-Fe$_3$S$_4$), and greigite (cubic spinel-Fe$_3$S$_4$).[1−3] Although there is considerable phase diversity, the situation is less complicated than the related oxides and their hydrolyzed species, which include wüstite (FeO), magnetite (Fe$_3$O$_4$), hemeatite (α,β-Fe$_3$O$_2$), maghemite (γ-Fe$_3$O$_2$), goethite (α-FeOOH), akaganéite (β-FeOOH), lepidocrocite (γ-FeOOH), feroxyhyte (δ-FeOOH), and ferrihydrite (Fe$_5$HO$_8 \cdot$4H$_2$O).[4]

Pyrite is a promising solar cell material because of its very high optical absorption coefficient of $\approx 5 \times 10^5$ cm^{-1} and useful band gap of 0.95 eV; it is also a cheap and relatively nontoxic material.[5] Its optical absorption coefficient is 2 orders of magnitude higher than that of crystalline silicon;[6] hence, only a thin layer is required in a solar cell based on this material.[7] It has also been used in commercial lithium primary cells[8,9] and high-temperature thermal batteries[10] and has been studied for use in secondary lithium cells.[11] Various methods have been employed to produce different phases of iron sulfide nanoparticles including high-energy mechanical milling combined with mechanochemical processing for FeS and FeS$_2$,[12] sulfur-reducing bacteria for Fe$_{1-x}$S and Fe$_3$S$_4$,[13,14] dendrimer-stabilized FeS,[15] laser pyrolysis of iron complexes for FeS,[16] reverse micelles for FeS$_2$,[17] solvothermal synthesis of Fe$_3$S$_4$,[18] polymer-stabilized wet chemical synthesis of FeS,[19]

---

*To whom correspondence should be addressed. E-mail:paul.obrien@manchester.ac.uk.

(1) Vaughan, D. J.; Lennie, A. R. *Sci. Prog.* (*Edinburgh*) **1991**, *75*, 371.

(2) Goodenough, J. B. *Mater. Res. Bull.* **1978**, *13*, 1305.

(3) Rao, C. N. R.; Pisharody, K. P. R. *Prog. Solid State Chem.* **1975**, *10*, 207.

(4) Cornell, R. M.; Schwertmann, U. VCH: Weinheim, Germany, 1996.

(5) Hopfner, C.; Ellmer, K.; Ennaoui, A.; Pettenkofer, C.; Fiechter, S.; Tributsch, H. *J. Cryst. Growth* **1995**, *151*, 325.

(6) Ennaoui, A.; Fiechter, S.; Pettenkofer, C.; Alonso-Vante, N.; Büker, K.; Hopfner, C.; Tributsch, H. *Sol. Energy Mater. Sol. Cells* **1993**, *29*, 289.

(7) Oertel, J.; Ellmer, K.; Bohne, W.; Röhrich, J.; Tributsch, H. *J. Cryst. Growth* **1999**, *198*, 1205.

(8) Tryk, D. A.; Kim, S.; Hu, Y.; Xing, X.; Scherson, D. A.; Antonio, M. R.; Leger, V. Z.; Blomgren, G. E. *J. Phys. Chem.* **1995**, *99*, 3732.

(9) Shao-Horn, Y.; Osmialowski, S.; Horn Quinn, C. *J. Electrochem. Soc.* **2002**, *149*, A1499.

(10) Henriksen, G. L.; Vissers, D. R.; Hilenskas, A. A. *J. Power Sources* **1995**, *54*, 134.

(11) Golodnitsky, D.; Peled, E. *Electrochim. Acta* **1999**, *45*, 335.

(12) Chin, P. P.; Ding, J.; Yi, J. B.; Liu, B. H. *J. Alloys Compd.* **2005**, *390*, 255.

(13) Watson, J. H. P.; Cressey, B. A.; Roberts, A. P.; Ellwood, D. C.; Charnock, J. M.; Soper, A. K. *J. Magn. Magn. Mater.* **2000**, *214*, 13.

(14) Watson, J. H. P.; Ellwood, D. C.; Soper, A. K.; Charnock, J. M. *J. Magn. Magn. Mater.* **1999**, *203*, 69.

(15) Shi, X.; Sun, K.; Balogh, L. P.; Baker, J. R., Jr. *Nanotechnology* **2006**, *17*, 4554.

(16) Bi, X. X.; Eklund, P. C. *Mater. Res. Soc. Symp. Proc.* **1993**, *286*, 161.

(17) Wilcoxon, J. P.; Newcomer, P. P.; Samara, G. A. *Solid State Commun.* **1996**, *98*, 581.

(18) Cao, F.; Hu, W.; Zhou, L.; Shi, W.; Song, S.; Lei, Y.; Wang, S.; Zhang, H. *Dalton Trans.* **2009**, 9246.

(19) Paknikar, K. M.; Nagpal, V.; Pethkar, A. V.; Rajwade, J. M. *Sci. Tecnol. Adv. Mater.* **2005**, *6*, 370.

and the decomposition of single-source precursors for FeS_2,[20] Fe_3S_4, and Fe_7S_8.[21,22]

Thin films of iron sulfide have also been prepared by the techniques of atmospheric- or low-pressure metal−organic chemical vapor deposition (AP or LP-MOCVD; FeS_2),[23−26] sulfurization of iron oxides (FeS_2),[27,28] flash evaporation (FeS_2),[29] ion beam and reactive sputtering (FeS_2),[30] plasma-assisted sulfurization of iron (FeS_2),[31] vapor transport (FeS_2),[32] chemical spray pyrolysis (FeS_2),[33] and vacuum thermal evaporation (FeS_2).[34] Among the methods used, MOCVD is one of considerable potential technological importance. Iron disulfide (FeS_2) thin films were prepared by Schleigh and Chang using iron pentacarbonyl [$Fe(CO)_5$], hydrogen sulfide, and *tert*-butyl sulfide as precursors by LPCVD.[23] Meester et al. also prepared iron disulfide (FeS_2) using iron(III) acetylacetonate [$Fe(acac)_3$], *tert*-butyl disulfide, and hydrogen.[35] There have been a very limited number of iron complexes employed as single-source precursors for the deposition of iron sulfide as $Fe_{1+x}S$, FeS_2, and $Fe_{1-x}S$ thin films, which include dithiocarbamato complexes $\{Fe(S_2CNRR')_3\}$ (R, R′ = Et, Et,[36] Me, ^{i}Pr[37]) and the sulfur-bridged binuclear iron carbonyl complex $\{Fe_2(CO)_6(\mu\text{-}S_2)\}$.[38]

To the best of our knowledge, there are no reports for the use of iron thiobiuret complexes as a single-source precursor for the preparation of iron sulfide thin films or nanoparticles. Herein we report the synthesis of four iron(III) complexes with 1,1,5,5-tetraalkyl-2-thiobiuret (alkyl = methyl, ethyl, and isopropyl) and the single-crystal X-ray structures of complexes **1**, **2**, and **4** and their use as single-source precursors for the deposition of iron sulfide (FeS and FeS_2) thin films by aerosol-assisted chemical vapor deposition (AACVD).

Experimental Section

All preparations were performed under an inert atmosphere of dry nitrogen using standard Schlenk techniques. All reagents were purchased from Sigma-Aldrich Chemical Co. and used as received. Solvents were distilled prior to use. IR spectra were recorded on a Specac single-reflectance ATR instrument (4000−400 cm^{-1} and resolution 4 cm^{-1}). Elemental analysis was performed by The University of Manchester microanalytical laboratory. Thermogravimetric analysis (TGA) measurements were carried out by a Seiko SSC/S200 model under a heating rate of 10 °C min^{-1} under nitrogen. Magnetic measurements were performed in the temperature range 1.9−300 K, by using a Quantum Design MPMS-XL SQUID magnetometer equipped with a 7 T magnet. The diamagnetic corrections for the compounds were estimated using Pascal's constants, and magnetic data were corrected for diamagnetic contributions of the sample holder.

Synthesis of $Fe(SON(CN^iPr_2)_2)_3$ (1). A solution of diisopropylcarbamoyl chloride (1.0 g, 6 mmol) and sodium thiocyanate (0.49 g, 6 mmol) in acetonitrile (25 mL) was heated to reflux with continuous stirring for 1 h, during which time a fine precipitate of sodium chloride formed. To the cooled reaction mixture was added diisopropylamine (1.49 mL, 12 mmol), followed by stirring for 30 min and the addition of a methanolic solution (10 mL) of iron nitrate (0.82 g, 2 mmol). The crude product precipitated as a red powder and was recrystallized from tetrahydrofuran (THF) to give shiny red needles, which were identified as **1**. Yield: 0.95 g (15%). Mp: 160 °C. IR (ν_{max}/cm^{-1}): 2956(w), 1494(s), 1425(s), 1353(s), 1278(s), 1142(s), 1060(s), 1038(s). Elem anal. Calcd for $C_{42}H_{84}N_9S_3O_3Fe$: C, 55.1; H, 9.1; N, 13.7; S, 10.5; Fe, 6.1. Found: C, 54.8; H, 8.9; N, 13.2; S, 9.9; Fe, 5.9.

Synthesis of $Fe_2(\mu\text{-}OMe)_2(SON(CNEt_2)_2)_2$ (2). The above procedure was used to prepare **2** but diethylamine (1.26 mL, 12 mmol) was used, which gave dark-brown crystals of **2** as a dimer. Yield: 0.80 g (11%). Mp: 140 °C. IR (ν_{max}/cm^{-1}): 2974(w), 2925(w), 1503(m), 1470(s), 1417(s), 1397(s), 1350(s), 1253(s), 1123(m), 1076(s), 1040(s). Elem anal. Calcd for $C_{42}H_{66}N_{12}S_4O_6Fe_2$: C, 46.9; H, 6.1; N, 15.6; S, 11.9; Fe, 10.4. Found: C, 46.5; H, 6.4; N, 15.3; S, 11.4; Fe, 10.2.

Synthesis of $Fe(SON(CNEt_2)_2)_3$ (3). The procedure for **1** was used to prepare **3** but with an excess of diethylamine (3.78 mL, 36 mmol), and a dark-red powder (**3**) resulted. Yield: 1.20 g (25%). Mp: 131 °C. IR (ν_{max}/cm^{-1}): 2971(w), 2929(w), 1497(s), 1424(s), 1396(s), 1349(s), 1254(s), 1125(s), 1075(s), 1048(s). Elem anal. Calcd for $C_{30}H_{60}N_9S_3O_3Fe$: C, 45.3; H, 7.5; N, 15.8; S, 24.1; Fe, 7.0. Found: C, 45.1; H, 7.7; N, 15.4; S, 23.7; Fe, 7.2.

Synthesis of $Fe(SON(CNMe_2)_2)_3\cdot{}^4/_3THF$ (4) and $Fe(SON(CNMe_2)_2)_3$ (4a). The process for **1** was followed but using dimethylamine in water (0.92 mL, 12 mmol), followed by recrystallization from THF, which gave a dark-red powder (**4**). Yield: 0.82 g (19%). Mp: 155 °C. IR (ν_{max}/cm^{-1}): 2851(w), 1529(s), 1465(s), 1378(s), 1341(s), 1192(m), 1022(s). Elem anal. Calcd for $C_{23.33}H_{46.67}N_9S_3O_{4.33}Fe$: C, 41.4; H, 6.9; N, 18.6; S, 14.2; Fe, 8.2. Found: C, 40.8; H, 6.5; N, 18.2; S, 13.5; Fe, 8.5.

The same experiment with dimethylamine in methanol (0.92 mL, 12 mmol) instead of water gave a dark-red powder (**4a**). Yield: 0.61 g (17%). Mp: 148 °C. IR (ν_{max}/cm^{-1}): 2851(w), 1529(s), 1465(s), 1378(s), 1341(s), 1192(m), 1112(s), 1022(s). Elem anal. Calcd for $C_{18}H_{36}N_9S_3O_3Fe$: C, 37.3; H, 6.2; N, 21.8; S, 16.6; Fe, 9.6. Found: C, 37.1; H, 6.4; N, 21.2; S, 16.3; Fe, 9.3.

X-ray Crystallography. Single-crystal X-ray diffraction (XRD) data for the compounds were collected using graphite-monochromated Mo Kα radiation (λ = 0.710 73 Å) on a Bruker APEX diffractometer. The structure was solved by direct methods and refined by full-matrix least squares[39] on F^2 All non-hydrogen atoms were refined anisotropically. Hydrogen atoms were included in calculated positions, assigned isotropic thermal parameters, and allowed to ride on their parent carbon atoms. All calculations were carried out using the *SHELXTL* package.[40] The details pertaining

---

(20) Chen, X.; Wang, Z.; Wang, X.; Wan, J.; Liu, J.; Qian, Y. *Inorg. Chem.* **2005**, *44*, 951.

(21) Vanitha, P. V.; O'Brien, P. *J. Am. Chem. Soc.* **2008**, *130*, 17256.

(22) Han, W.; Gao, M. *Cryst. Growth Des.* **2008**, *8*, 1023.

(23) Schleigh, D. M.; Chang, H. S. W. *J. Cryst. Growth* **1991**, *112*, 737.

(24) Thomas, B.; Hoepfner, C.; Ellmer, K.; Fiechter, S.; Tributsch, H. *J. Cryst. Growth* **1995**, *146*, 630.

(25) Thomas, B.; Cibik, T.; Hoepfner, C.; Diesner, D.; Ehlers, G.; Fiechter, S.; Ellmer, K. *J. Mater. Sci.* **1998**, *9*, 61.

(26) Meester, B.; Reijnen, L.; Goossens, A.; Schoonman, J. *J. Phys. (Paris)* **1999**, *9*, Pr8–613.

(27) Smestad., G.; Ennaoui, E.; Fiechter, S.; Tributsch, H.; Hofman, W. K.; Birkholz, M. *Sol. Energy Mater.* **1990**, *20*, 149.

(28) Ouertani, B.; Ouerfelli, J.; Saadoun, M.; Bessais, B.; Ezzaouia, H.; Bernede, J. C. *Mater. Charact.* **2005**, *54*, 431.

(29) Ferrer, I. J.; Sanchez, C. J. *Appl. Phys.* **1991**, *70*, 2641.

(30) Birkholz, M.; Lichtenberger, D.; Hoepfner, C.; Fiechter, S. *Sol. Energy Mater. Sol. Cells* **1992**, *27*, 243.

(31) Bausch, S.; Sailer, B.; Keppner, H.; Willeke, G.; Bucher, E.; Frommeyer, G. *Appl. Phys. Lett.* **1990**, *25*, 57.

(32) Ennaoui, A.; Schlichtlorel, G.; Fiechter, S.; Tributsch, H. *Sol. Energy Mater. Sol. Cells* **1992**, *25*, 169.

(33) Smestad, G.; Da Silva, A.; Tributsch, H.; Fiechter, S.; Kunst, M.; Meziani, N.; Birkholz, M. *Sol. Energy Mater.* **1989**, *18*, 299.

(34) Rezig, B.; Dalma, H.; Kanzai, M. *Renewable Energy* **1992**, *2*, 125.

(35) Meester, B.; Reijnen, L.; Goossens, A.; Schoonman, J. *Chem. Vap. Deposition* **2000**, *6*, 121.

(36) Soon, J. M.; Goh, L. Y.; Loh, K. P.; Foo, Y. L.; Ming, L.; Ding, J. *Appl. Phys. Lett.* **2007**, *91*, 084105.

(37) O'Brien, P.; Otway, D. J.; Park, J. H. *Mater. Res. Soc. Symp. Proc.* **2000**, *606*, 133.

(38) Shyu, S. G.; Wu, J. S.; Wu, C. C.; Chuang, S. H.; Chi, K. M. *Inorg. Chim. Acta* **2002**, *334*, 276.

(39) Sheldrick, G. M. *SHELXS-97* and *SHELXL-97*; University of Göttingen: Göttingen, Germany, 1997.

(40) Bruker. *SHELXTL*, version 6.12; Bruker AXS Inc.: Madison, WI, 2001.

to the data collection of the crystals are as follows. **1**: $C_{44}H_{87}N_{10}O_3S_3Fe$, M = 956.27, dark-brown needles, monoclinic, space group $P2(1)/n$, a = 14.341(3) Å, b = 15.224(3) Å, c = 25.725(4) Å, α = 90°, β = 97.144(4)°, γ = 90°, V = 5572.9(2) A^3, Z = 4, D = 1.140 Mg m^{-3}, T = 100(2) K, reflections collected = 31 561/11 281, unique reflections = R(int) = 0.0696, final R indices $[I > 2\sigma(I)]$ R1 = 0.0414 and wR2 = 0.0622, R indices (all data) R1 = 0.0923 and wR2 = 0.0674, largest diff peak and hole = +0.661 and −0.409 e A^{-3}, GOF = 0.709. **2**: $C_{42}H_{86}N_{12}O_6S_4Fe_2$, M = 1095.17, dark-brown blocks, monoclinic, space group $P2(1)/c$, a = 10.466(2) Å, b = 25.355(4) Å, c = 10.328(3) Å, α = 90°, β = 95.442(3)°, γ = 90°, V = 2728.5(8) A^3, Z = 2, D = 1.333 Mg m^{-3}, T = 100(2) K, reflections collected = 15 681/5558, unique reflections = R(int) = 0.0313, final R indices $[I > 2\sigma(I)]$ R1 = 0.0510 and wR2 = 0.1160, R indices (all data) R1 = 0.0598 and wR2 = 0.1197, largest diff peak and hole = +1.677 and −0.370 e A^{-3}, GOF = 1.144. **4**: $C_{23.33}H_{46.67}N_9O_{4.33}S_3Fe$, M = 674.73, red plates, orthorhombic, space group $Pna2(1)$, a = 16.978(5) Å, b = 31.180(1) Å, c = 18.160(5) Å, α = 90°, β = 90°, γ = 90°, V = 9613(5) A^3, Z = 12, D = 1.399 Mg m^{-3}, T = 100(2) K, reflections collected = 23 094/11 030, unique reflections = R(int) = 0.1081, final R indices $[I > 2\sigma(I)]$ R1 = 0.1006 and wR2 = 0.2098, R indices (all data) R1 = 0.1535 and wR2 = 0.2358, largest diff peak and hole = +1.196 and −0.546 e A^{-3}, GOF = 1.010. **4a**: $C_{18}H_{36}N_9O_3S_3Fe$, M = 578.59, brown blocks, tetragonal, space group $P4/n$, a = 25.519(1)Å, b = 25.519(1) Å, c = 16.953(3) Å, α = 90°, β = 90°, γ = 90°, V = 11041.3(1) A^3, Z = 16, D = 1.392 Mg m^{-3}, T = 100(2) K, reflections collected = 78 789/9765, unique reflections = R(int) = 0.1600, final R indices $[I > 2\sigma(I)]$ R1 = 0.0770 and wR2 = 0.2120, R indices (all data) R1 = 0.1638 and wR2 = 0.2568, largest diff peak and hole = +5.508 and −0.563 e A^{-3}, GOF = 0.961. CCDC reference numbers 715964, 715969, 776449, and 776450. The atomic coordinates for these structures have been deposited with the Cambridge Crystallographic Data Centre. The coordinates can be obtained, upon request, from the Director, Cambridge Crystallographic Data Centre, 12 Union Road, Cambridge CB2 1EZ, U.K.

Deposition of Films by AACVD. In a typical deposition, 0.20 g of the precursor was dissolved in 20 mL of THF in a two-necked 100 mL round-bottomed flask with a gas inlet that allowed the carrier gas (argon) to pass into the solution to aid the transport of aerosol. This flask was connected to the reactor tube by a piece of reinforced tubing. The argon flow rate was controlled by a Platon flow gauge. Seven glass substrates (approximately 1 × 3 cm) were placed inside the reactor tube, which is placed in a Carbolite furnace. The precursor solution in a round-bottomed flask was kept in a water bath above the piezoelectric modulator of a Pifco ultrasonic humidifier (model 1077). The aerosol droplets of the precursor thus generated were transferred into the hot wall zone of the reactor by a carrier gas. Both the solvent and precursor were evaporated, and the precursor vapor reached the heated substrate surface where thermally induced reactions and film deposition took place.

Characterization of Thin Films. XRD studies were performed on a Bruker AXS D8 diffractometer using Cu Kα radiation. The samples were mounted flat and scanned between 20 and 80° in a step size of 0.05 with a count rate of 9 s. Films were carbon-coated using an Edwards E306A coating system before scanning electron microscopy (SEM) and energy-dispersive X-ray (EDX) analyses were carried out. SEM analysis was performed using a Philips XL 30FEG instrument, and EDX was carried out using a DX4 instrument. Transmission electron microscopy (TEM) analysis was performed using a cm200 instrument. Atomic force microscopy (AFM) analysis was carried using a Veeco CP2 instrument. The X-ray photoelectron spectroscopy (XPS) spectra were recorded using a Kratos Axis Ultra spectrometer employing a monochromated Al Kα X-ray source and an analyzer pass energy of 80 eV for survey scans and 20 eV for elemental scans, resulting in a total energy resolution of ca. 1.2 or 0.9 eV, respectively. Uniform charge neutralization of the photoemitting surface was achieved by exposing the surface to low-energy electrons in a magnetic immersion lens system (Kratos Ltd.). The system base pressure was 1×10^{-9} mbar. Spectra were analyzed by first subtracting a Shirley background and then obtaining accurate peak positions by fitting peaks using a mixed Gaussian/Lorenzian line shape. During fitting, spin−orbit split components were constrained to have identical line widths, elemental spin−orbit energy separations, and theoretical spin−orbit area ratios. All photoelectron binding energies (BEs) are referenced to a C 1s adventitious peak set at 285 eV BE. The analyzer was calibrated using elemental references: Au $4f_{7/2}$ (83.98 eV BE), Ag $3d_{5/2}$ (368.26 eV BE), and Cu $2p_{3/2}$ (932.67 eV BE).

Scheme 1. Schematic Representation of the Synthesis of Ligands and Complexes **1**−**4**

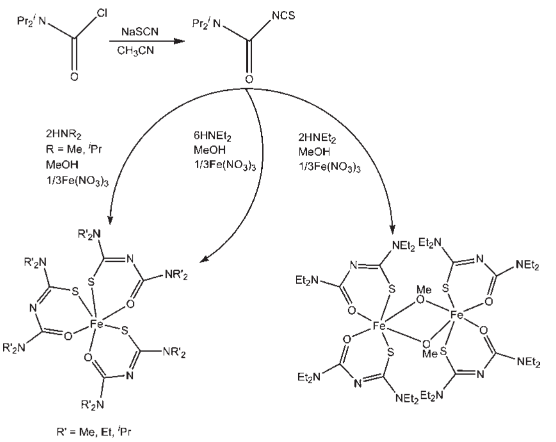

Results and Discussion

The reaction of diisopropylcarbamoyl chloride, sodium thiocyanate, and diisopropylamine followed by the addition of a methanolic solution of iron nitrate gave a red crystalline powder of complex **1**. The same reaction with diethylamine gave dark-brown crystals of dimeric complex **2**. The reaction with an excess of diethylamine gave a dark-red powder of complex **3**. Complex **4** was isolated as a powder after evaporation of the solvent or as a THF solvate after recrystallization from THF. A representation of the syntheses is given in Scheme 1. All four complexes are low-melting solids and are air- and moisture-stable for several weeks. Complexes **1**−**4** are soluble in most organic solvents (toluene, THF, chloroform, and dichloromethane), which makes them suitable for AACVD.

The synthesis of complex **2** was repeated many times under varying reaction conditions; for example, the addition of water and/or the use of twice as much diethylamine in the reaction mixture did not stop the methoxy-bridged compound from forming. However, when the reaction was carried out with a 3-fold excess of diethylamine, the monomer formed, but all attempts to crystallize this complex for single-crystal X-ray studies were unsuccessful. The reasons for this unusual but reproducible behavior are not at this time clear to us.

Single-Crystal X-ray Structure of 1. The single-crystal X-ray structure of complex **1** (Figure 1a) shows an iron(III) ion in a distorted octahedral environment with a S_3O_3 donor set. The donor atoms, three sulfur and three oxygen atoms, are in a facial arrangement. The *fac* isomer is statistically preferred and often predominates in systems of this type with S_3O_3 sets at iron(III).[41,42] The bite

---

(41) Ahmed, J.; Ibers, J. A. *Inorg. Chem.* **1977**, *16*, 935.
(42) Hoskins, B. F.; Pannan, C. D. *Inorg. Nucl. Chem. Lett.* **1975**, *11*, 409.

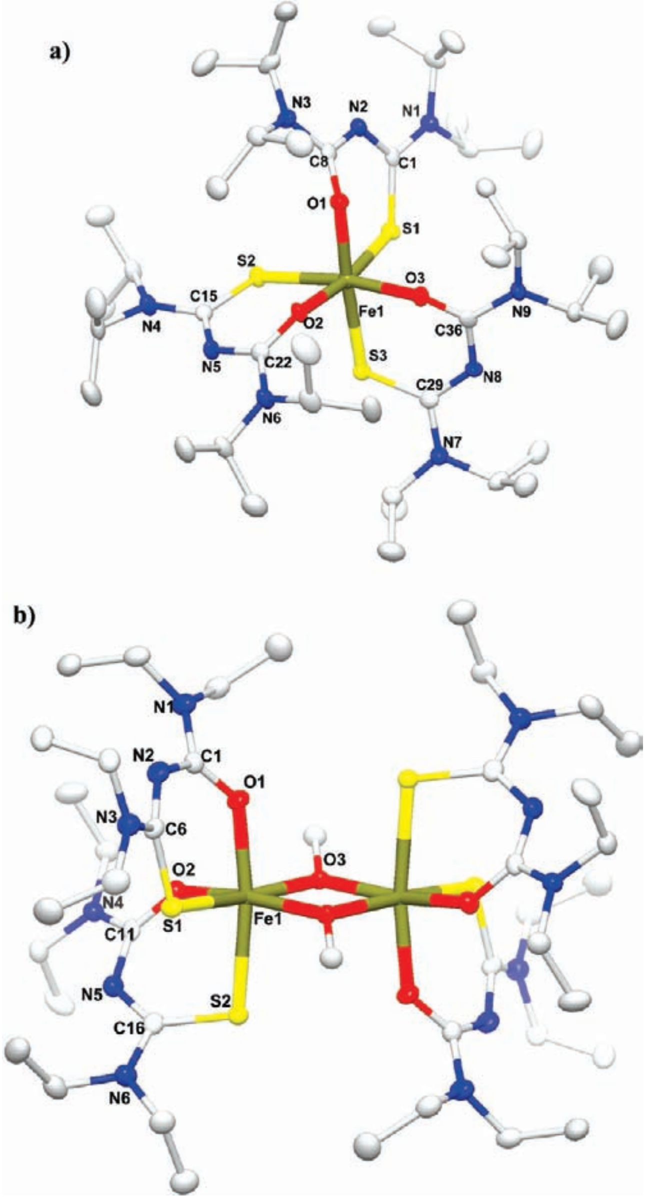

Figure 1. (a) Single-crystal X-ray structure of **1**. Selected bond lengths (Å) and bond angles (deg): Fe1−O1 1.986(2), Fe1−S1 2.418(8), O1−C8 1.276(3), S3−C29 1.746(3); O3−Fe1−S3 85.90(5), C1−N2−C8 123.8(2), O1−C8−N2 126.3(2). (b) Single-crystal X-ray structure of **2**. Selected bond lengths (Å) and bond angles (deg): Fe1−O1 1.993(2), Fe1−O3 1.988(2), Fe1−S1 2.424(8), S1−C6 1.753(3); O3−Fe1−O1 100.94(8), O3−Fe1−S1 94.85. The unlabeled atoms are symmetrically related to the labeled atoms.

angles of O1−Fe1−S1, O2−Fe1−S2, and O3−Fe1−S3 are 86.54(5)°, 86.40(5)°, and 85.90(5)°, indicating a distorted octahedral geometry on iron(III). Each thiobiuret ligand chelates to form three six-membered rings (NC$_2$OSFe), with Fe−S bond distances ranging from 2.412(8) to 2.418(8) Å and Fe−O bond distances ranging from 1.972(2) to 1.986(2) Å. This is somewhat larger than the bond lengths of M−S and M−O observed for cobalt and nickel complexes of the same ligand.[43] Structure refinement data are given in the Experimental Section, and selected bond lengths and angles are given in the caption to Figure 1a.

Single-Crystal X-ray Structure of 2. The complex crystallizes in the monoclinic space group $P2_1/c$. Each iron ion is chelated by two bidentate ligands and bridged by two methoxide ions and is in a distorted octahedral coordination with a S$_2$O$_4$ donor set. The two sets of ligands coordinated to each iron(III) are trans. Within each of the two thiobiuret ligands, the four atoms of the urea or thiourea groups are close to being coplanar. Both thiobiuret ligands on each unit chelate to form two six-membered rings (NC$_2$OSFe), with Fe−S bond distances ranging from 2.424(8) to 2.450(9) Å and Fe−O bond distances ranging from 1.993(2) to 2.011(2) Å. The Fe1−O3 distance 1.988(2) Å is similar to that reported for Fe$_2$(μ-OCH$_3$)$_2$(HL)$_4$, where H$_2$L is 2-salicyloylhydrazono-1,3-dithiolane [1.974(2) Å].[44] The pattern of bond distances in all four ligands indicates that the formal negative charge is predominantly localized on the sulfur atom. The relatively long C−S and short C−O average bond lengths of 1.753(8) and 1.282(3) Å are consistent with predominantly single- or double-bond character, respectively, and this bond localization is also reflected in the average C−N bond distances to the central N2 atom: 1.323(4) Å in the (iso)thiourea group and 1.336(4) Å in the urea group (Figure 1b). Structure refinement data are given in the Experimental Section, and selected bond lengths and angles are given in the caption to Figure 1b.

Single-Crystal X-ray Structure of 4 and 4a. The single-crystal X-ray structure of complex **4** reveals a distorted octahedral geometry at the iron(III) ion through three sulfur and three oxygen atoms of the thiobiuret ligands (Figure 2). The complex crystallizes in two forms depending on the methods of synthesis and recrystallization. Orthorhombic crystals [*Pna*2(1)] of **4** were obtained when the reaction was carried out using dimethylamine in water, followed by recrystallization from THF. In this form, three molecules of the complex were present in the unit cell along with four molecules of the THF solvent, whereas tetragonal crystals ($P4/n$) of **4a** were obtained directly from the reaction carried out using dimethylamine in methanol instead of water. There are no significant differences in the atomic separations between complex **4** or **4a** and **1**. Structure refinement data are given in the Experimental Section, and selected bond lengths and angles are given in the caption to Figure 2.

TGA. TGA provides an understanding of the decomposition process and the volatility of the complexes. TGA of the complexes **1**, **3**, and **4** indicates single-step decomposition with a rapid weight loss between 128 and 208, 117 and 312, and 113 and 309, respectively (Supporting Information). The solid decomposition residue amounts to 20.0% for **1**, which is in fair agreement with the calculated value of 22.7% for Fe$_2$S$_3$. Similarly, the observed final residue of 27.1% for **3** is in agreement with the calculated value of 27.7% for Fe$_2$S$_3$, and the weight of the final residue is 13.0% for **4**, close to the calculated value of 15.0% for FeS, whereas complex **2** decomposes in two steps with rapid weight loss at temperatures between 117 and 195 °C and between 195 and 245 °C. The weight loss of 5.9% in the first step is in good agreement with that

---

[43] Ramasamy, K.; Malik, M. A.; O'Brien, P.; Raftery, J. *Dalton Trans.* **2010**, *39*, 1460.

[44] Bouslimani, N.; Clement, N.; Rogez, G.; Turek, P.; Bernard, M.; Dagorne, S.; Martel, D.; Cong, H. N.; Welter, R. *Inorg. Chem.* **2008**, *47*, 7623.

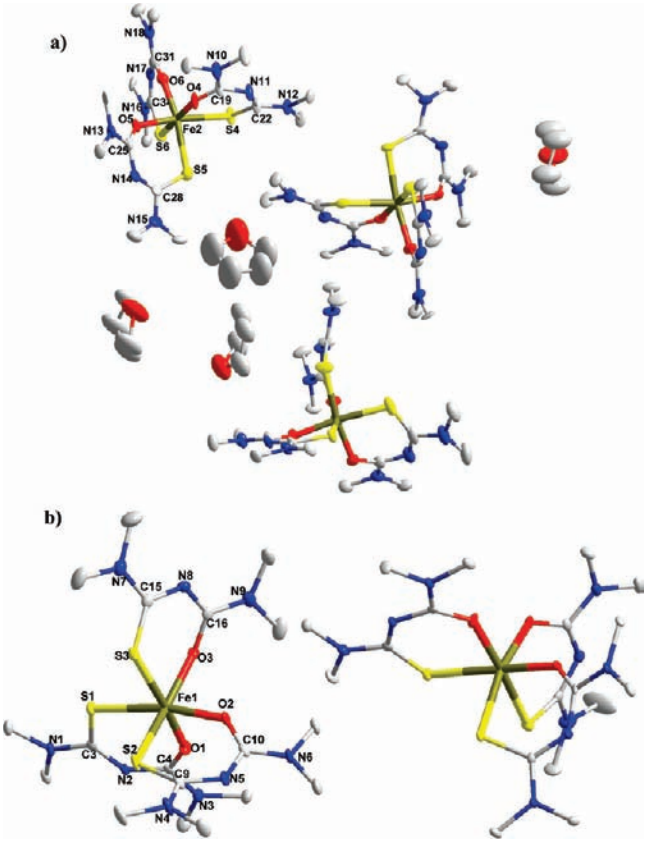

Figure 2. Single-crystal X-ray structures of **4**. (a) Orthorhombic system. Selected bond lengths (Å) and bond angles (deg): Fe1−O1 1.990(1), Fe1−O3 2.053(1), Fe1−S1 2.421(5), S1−C4 1.700(2); O1−Fe1−S1 85.5(3), C1−N1−C2 119.6(1). (b) Tetragonal system. Selected bond lengths (Å) and bond angles (deg): Fe1−O1 1.961(1), Fe1−O3 2.018(9), Fe1−S1 2.413(3), S1−C3 1.729(9); O1−Fe1−S1 86.5(2), C3−N1−C1 123.0(8).

calculated for two units of methoxides (6.0%). The remaining residue amounts to 17.2%, which is close to the calculated value of 18.9% for Fe_2S_3.

Magnetic Measurements on 2. We have investigated the magnetic properties of a polycrystalline sample of compound **2**, which is a di-μ-methoxo-bridged iron(III) dinuclear complex, over the temperature range 1.8−300 K under applied magnetic fields of 1, 5, and 10 kOe. The temperature dependence of χ_M and $\chi_M T$ (where χ_M represents the molar magnetic susceptibility) of **2** recorded with a magnetic field of 1 kOe is presented in Figure 3.

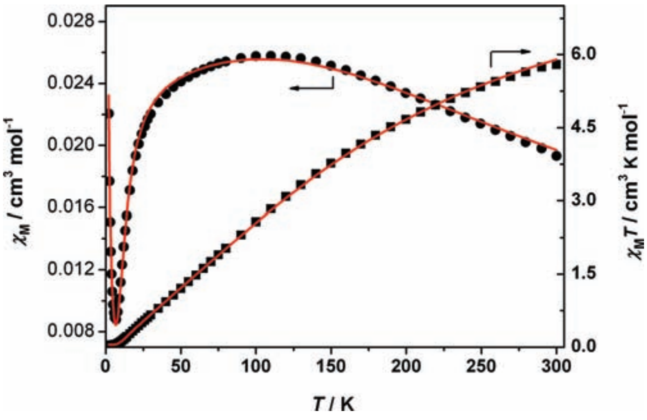

Figure 3. χ_M (circles) and $\chi_M T$ (squares) as a function of the temperature for complex **2**. The solid red lines correspond to the fits of the $\chi_M = f(T)$ curve and to the corresponding $\chi_M T$ product, using the parameters given in the text.

The $\chi_M T$ value at room temperature is 5.79 cm^3 K mol^{-1}, which is well below the spin-only value of 8.75 cm^3 K mol^{-1} (assuming $g = 2$) expected for two noninteracting high-spin iron(III) metal ions. Upon cooling, the $\chi_M T$ product decreases continuously down to almost zero (0.03 cm^3 K mol^{-1} at 1.8 K). This indicates relatively strong antiferromagnetic coupling between metal centers, leading to a diamagnetic ($S = 0$) spin ground state. Indeed, the susceptibility curve reaches a maximum value of 0.026 cm^3 mol^{-1} at 100 K and decreases upon further cooling to approach zero ($\chi_M = 0.0087$ cm^3 mol^{-1}) at 7 K. Below 7 K, however, the susceptibility curve increases again to reach 0.022 cm^3 mol^{-1} at 1.8 K, suggesting the presence of a small amount of paramagnetic impurity. In order to quantify the intramolecular antiferromagnetic coupling between the two iron(III) centers, the experimental susceptibility data were analyzed by means of the Van Vleck equation (1):[45]

$$\chi_M = \frac{2Ng^2\beta^2}{k_B T}\,\frac{e^x + 5e^{3x} + 14e^{6x} + 30e^{10x} + 55e^{15x}}{1 + 3e^x + 5e^{3x} + 7e^{6x} + 9e^{10x} + 11e^{15x}}(1-\rho) + \frac{35Ng^2\beta^2}{6k_B T}\rho \qquad (1)$$

where $x = 2J/k_B T$, which is derived from the spin Hamiltonian $\mathbf{H} = -2JS_{Fe1}S_{Fe2} + g\beta HS$, where J is the exchange coupling parameter, ρ represents the proportion of a paramagnetic impurity considered to be an uncoupled iron(III) species ($S_{impur} = {}^5/_2$), and the spin operator S is defined as $S = S_{Fe1} + S_{Fe2}$. The least-squares fit to eq 1 leads to $J = -13.32$ cm^{-1}, $g = 2.04$, and $\rho = 0.005$, with an excellent reliability factor of 7.8×10^{-6}, defined as $R(\chi_M) = \sum(\chi_M{}^{obs} - \chi_M{}^{calc})^2/\sum(\chi_M{}^{obs})^2$. The same set of parameters reproduce very well the $\chi_M T$ data plotted in Figure 3. The negative sign of J confirms the occurrence of antiferromagnetic interactions in this compound. The size of the exchange coupling constant is in good agreement with the values reported in the literature for di-μ-methoxo-bridged diiron(III) complexes with similar structural features.[44]

AACVD of Iron Sulfide Thin Films from 1. Deposition was carried out at substrate temperatures from 300 to 450 °C with an argon flow rate of 160 sccm onto glass substrates. No deposits were obtained below 300 °C. Reflective dark-brown films were deposited at 300 and 350 °C, and black films were obtained at 400 and 450 °C. The powder XRD pattern of the as-deposited films at 300−450 °C (Figure 4) shows films of hexagonal troilite-2H FeS (ICDD no. 037-0477) with a smaller amount of tetragonal pyrrhotite $Fe_{1-x}S$ (ICDD no. 024-0079). At the lowest deposition temperature (300 °C), the XRD patterns of hexagonal troilite-2H planes of (112), (200), (302), and (304) were dominant along with a peak at 38.9° (2θ) corresponding to the (213) plane of tetragonal pyrrhotite. At the higher deposition temperature (450 °C), diffraction peaks of the (004), (201), (114), (214), and (304) planes from troilite become dominant. The XPS spectra from the thin film

---

(45) Kahn, O. *Molecular Magnetism*; VCH: New York, 1993; Chapter 6.

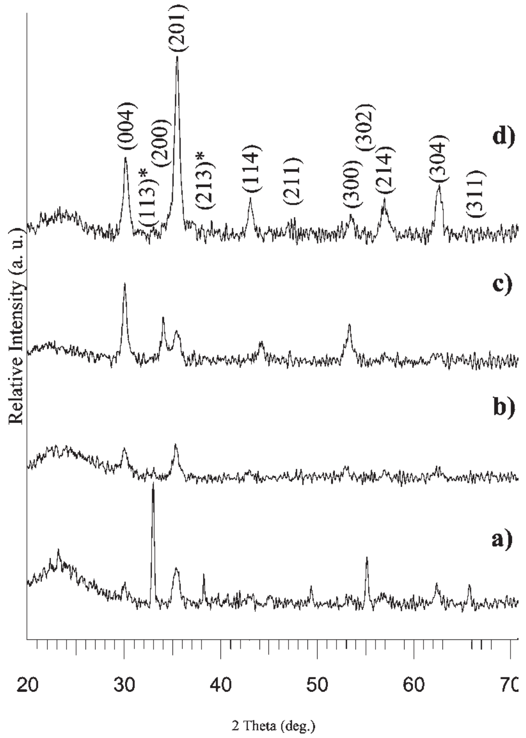

Figure 4. Powder XRD patterns of troilite (FeS) thin films deposited from **1** onto glass at (a) 300, (b) 350, (c) 400, and (d) 450 °C. The asterisk symbol denotes the pyrrhotite.

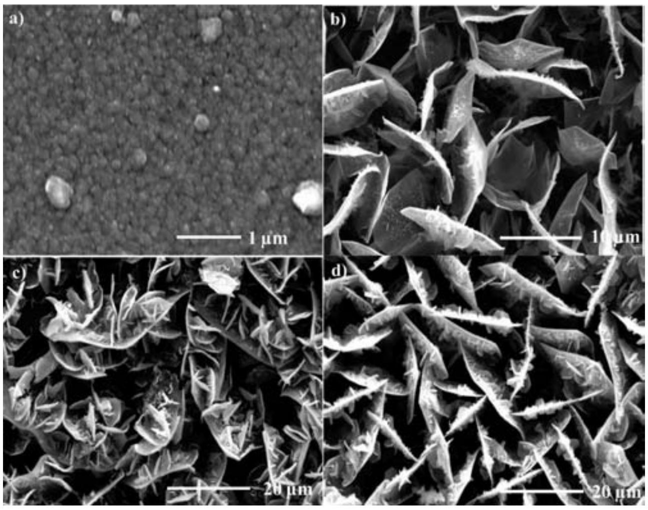

Figure 5. SEM images of iron sulfide (FeS) films deposited from **1** onto glass at (a) 300, (b) 350, (c) 400, and (d) 450 °C.

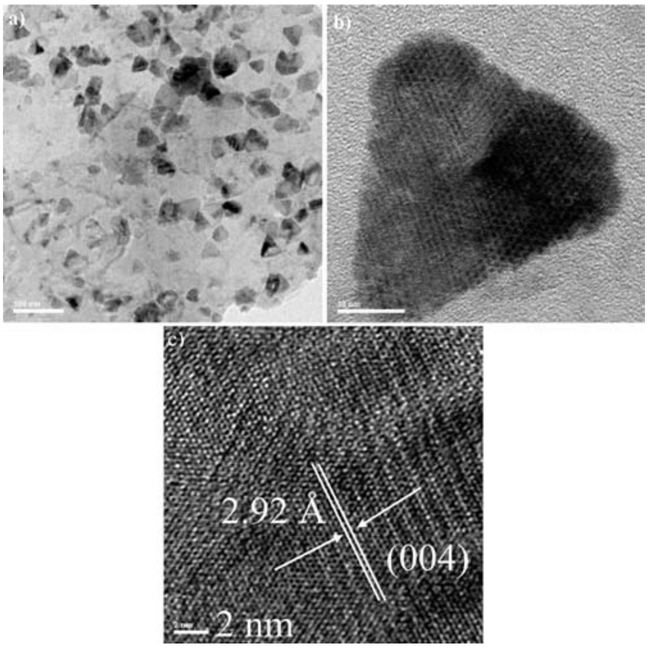

Figure 6. (a) Lower- and (b) higher-magnification TEM images of the FeS thin films deposited from **1** at 400 °C. (c) HRTEM image.

deposited at 400 °C show both unoxidized and oxidized forms of iron sulfide (Supporting Information). The BE of the Fe $2p_{3/2}$ peak is fitted with two components: iron oxide at 710.8 eV and iron sulfide at 707 eV. The peaks at 161.3 eV can be attributed to S 2p as sulfide, and those at 168 eV can be attributed to sulfur as sulfate.[46] The presence of oxides is expected because of handling of the sample in an open atmosphere. The presence of unoxidized iron sulfide suggests that the oxide is likely covered only to the film surface with a thickness of less than Fe 2p and S 2p electron escape depths (< 2 nm). This analysis also shows the presence of carbon (3.8%) and nitrogen (1.2%) on the films.

The SEM images in Figure 5 show the growth of smaller individual granular crystallites (size 300−400 nm) at 300 °C and layerlike crystallites at 350 °C, whereas plates of crystallites (size 20−25 μm) were formed at 400 and 450 °C. EDX analysis shows that the films are composed of iron/sulfur ratios of 51:49 (300 °C), 52:48 (350 °C), and 55:45 (400 and 450 °C). The Fe:S ratio is closer to 1:1 in the films deposited at 300 °C. Further insight into the morphology and microstructure of the films was gained by TEM. The TEM images from the scratched sample of films grown at 400 °C show that the films consist of trigonal plates, with sizes ranging from 35 to 45 nm, and also clearly exhibit the primary trigonal structures attached together in the regular manner to form secondary bigger crystallites (Figure 6a).

The higher magnified TEM image in Figure 6b shows smaller trigonal crystallites with sizes of 2−3 nm self-assembling to form trigonal crystals of larger size. The high-resolution TEM (HRTEM) image of the trigonal plates (Figure 6c) shows the lattice fringes with a *d* spacing of 0.29 nm corresponding to a (004) reflection of hexagonal FeS. The surface topography of the films analyzed by a 2D AFM image (Figure 7a) of films deposited at 300 °C shows well-interconnected globular crystallites. The average roughness value ranged from 16 to 26 nm for the films deposited at 300−450 °C. The increase in the surface roughness with increasing deposition temperature was associated with an increase of the grain size. As the grain grew bigger, the density of the grain boundaries decreased and the grain growth took place with a large variation in the height of the grain on the film surface. Therefore, it is apparent that the deposition temperature of the films changes the grain size as well as the surface roughness.

AACVD of Iron Sulfide Thin Films from 2. Iron sulfide thin film deposition was carried out at substrate temperatures between 250 and 400 °C with an argon flow rate of

---

(46) Wadia, C.; Wu, Y.; Gul, S.; Volkman, S. K.; Guo, J.; Alivisatos, P. *Chem. Mater.* **2009**, *21*, 2568.

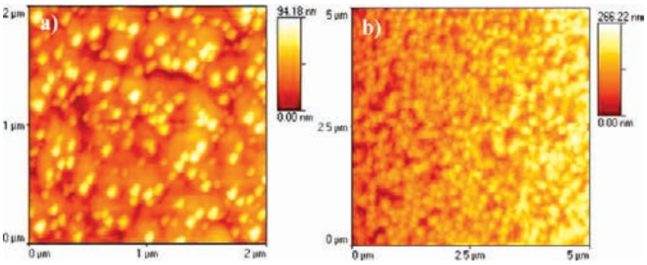

Figure 7. 2D AFM images: (a) FeS deposited at 300 °C from **1**; (b) FeS deposited at 350 °C from **2**.

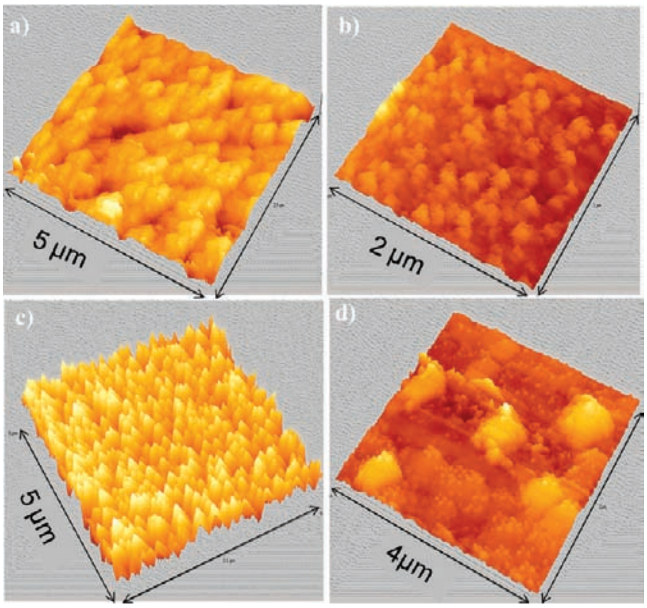

Figure 8. 3D AFM images: FeS films deposited as complexes **1**−**4** (a−d).

160 sccm using complex **2**. No deposition was obtained below 250 °C and above 400 °C. Reddish reflective films were deposited at 250 and 300 °C, whereas dark-brown films were deposited at 350 and 400 °C. XRD patterns of as-deposited films at 250−400 °C in Figure 9 show that the films consist of hexagonal troilite-2H FeS (ICDD no. 037-0477) and cubic pyrite FeS_2 (ICDD no. 042-1340). At the lowest deposition temperature (250 °C), only pyrite (FeS_2) diffraction peaks were observed, whereas hexagonal troilite (FeS) peaks become predominant at 300 °C. At 350 and 400 °C, almost equal amounts of troilite and pyrite were observed. This suggests that the loss of sulfur at higher deposition temperature leads to the formation of troilite FeS predominantly. The major diffraction peaks can be assigned to (200), (210), (211), and (311) of cubic pyrite and (004), (201), (204), and (301) of the hexagonal trolite-2H phase.

The morphology of as-deposited films was investigated by SEM, as shown in Figure 10. At 250 °C, smaller cluster-like crystallites with sizes ranging from 200 to 300 nm were obtained, whereas cross-linked networklike sheets (5−7 µm) were obtained at 300 °C. Flowerlike crystallites with sizes of 10−15 µm deposited at 350 and 400 °C. EDX analysis shows that the films are composed of iron/sulfur ratios of 52:48 (250 and 300 °C) and 55:45 (350 and 400 °C).

The TEM images from the scratched sample of films grown at 300 °C show that the films consist of plates with sizes ranging from 25 to 35 nm. The HRTEM image of the plates (Figure 11b) shows the lattice fringes with a *d* spacing of 0.27 nm corresponding to the (200) reflection of cubic FeS_2. The AFM image of films deposited from complex **2** onto a glass substrate in Figure 7b shows highly packed crystallites. The average roughness of the films ranged from 14 to 31 nm for the films deposited at 250−400 °C.

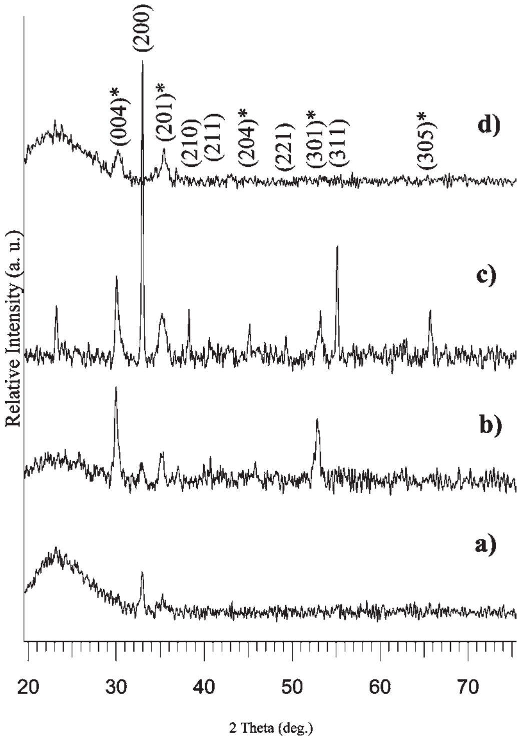

Figure 9. Powder XRD of pyrite iron sulfide thin films deposited from **2** onto glass at (a) 250, (b) 300, (c) 350, and (d) 400 °C. The asterisk symbol denotes the troilite-2H.

AACVD of Iron Sulfide Thin Films from 3. Thin films of iron sulfide deposited from complex **3** onto a glass substrate at temperatures between 300 and 450 °C. Brownish films deposited at 300 °C, whereas black films deposited at 350, 400, and 450 °C. The films characterized by powder XRD show the deposition of a mixture of troilite (ICDD no. 037-0477) and pyrite phases (ICDD no. 042-1340) at all temperatures, although the pyrite diffraction peaks are dominant at 400 °C. The major diffraction peaks could be indexed as (103), (110), (201), (205), and (220) of troilite and (200), (210), (211), (220), and (311) of pyrite (Supporting Information).

SEM images of films deposited at 300 °C show granular crystallites with an average size of 500−700 nm; a mixture of granular crystallites and hexagonal plates were deposited at 350 °C, whereas hexagonal plates were deposited in the *c* direction of the glass substrate at 400 and 450 °C with an average size of 5−7 µm (Figure 12). EDX analysis shows that the films are composed of iron/sulfur ratios 51:49 (300 °C), 52:48 (350 °C), and 55:45 (400 and 450 °C).

TEM images from the scratched sample of films grown at 400 °C further confirm the deposition of platelike crystallites (Figure 13). The AFM image in Figure 8c shows the growth of closely packed crystallites onto a glass substrate with an average roughness of 19−23 nm (300−450 °C).

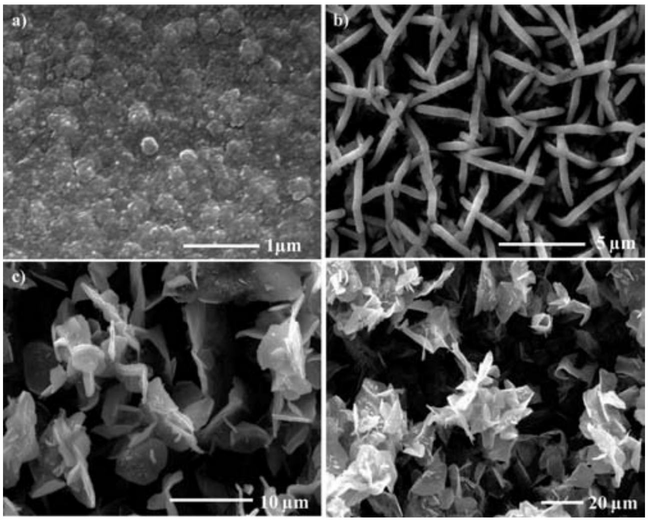

Figure 10. SEM images of pyrite iron sulfide films deposited from **2** onto glass at (a) 250, (b) 300, (c) 350, and (d) 400 °C.

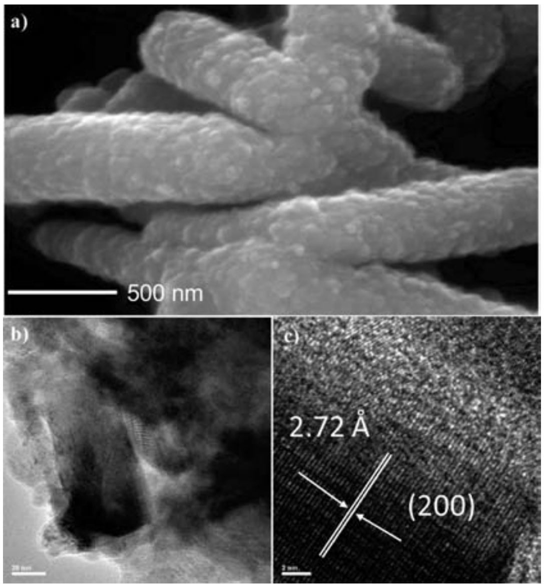

Figure 11. (a) HRSEM image of iron sulfide films deposited at 300 °C. (b) TEM image of the thin films deposited from **2** at 300 °C. (c) HRTEM image.

AACVD of Iron Sulfide Thin Films from 4. Reddish uniform reflective iron sulfide thin films were deposited from complex **4** at 350 and 400 °C. The films deposited were very thin so that the XRD pattern could not be obtained. SEM images in Figure 14 show the deposition of granular crystallites with sizes of 100−150 nm at 350 °C, whereas granular crystallites and rods of crystallites were obtained at 400 °C. EDX analysis shows that the films are composed of iron/sulfur ratios of 53:47 (350 °C) and 56:44 (400 °C). TEM images of scratched films deposited at 400 show nanospheres with an average size of 100−150 nm (Figure 15a) and nanorods with a width of 10 nm (Figure 15c).

The HRTEM image of the spherical crystallites (Figure 15d) shows the lattice fringes with a *d* spacing of 0.23 nm corresponding to the (111) reflection of tetragonal FeS. The surface topography of the films further

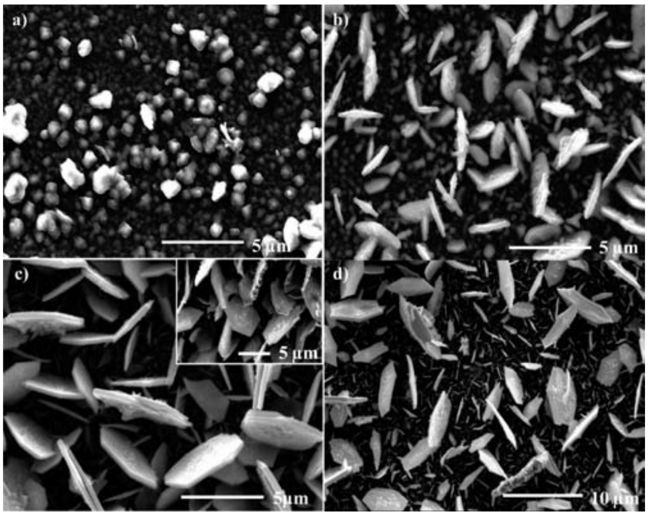

Figure 12. SEM images of troilite (FeS) iron sulfide films deposited from **3** onto glass at (a) 300, (b) 350, (c) 400, and (d) 450 °C and onset 45° tilt image of film deposited at 400 °C.

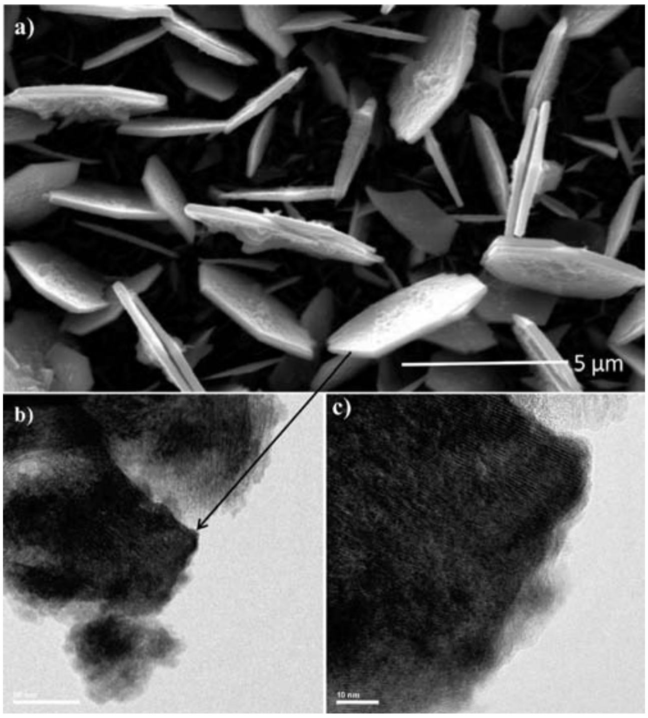

Figure 13. (a) Higher-magnification SEM image. (b) Lower- and (c) higher-magnification TEM images of the thin films deposited from **3** at 400 °C.

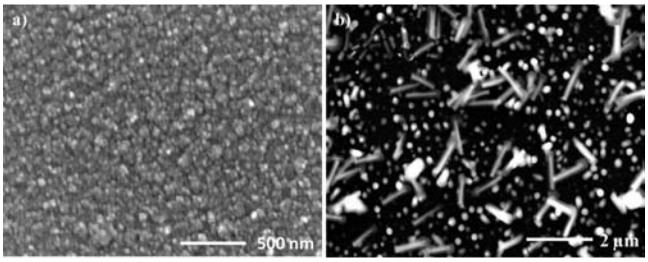

Figure 14. SEM images of iron sulfide films deposited from **4** onto glass at (a) 350 and (b) 400 °C.

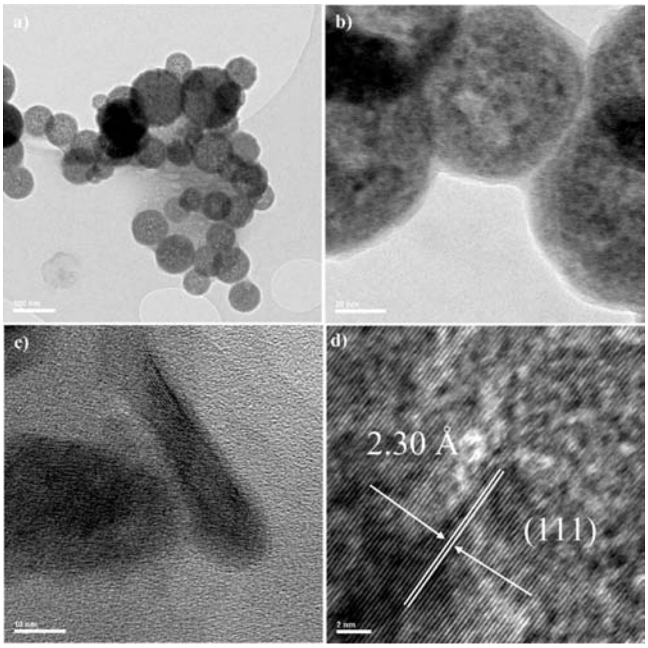

Figure 15. TEM images of the thin films deposited from **4** at 400 °C: (a) lower- and (b) higher-magnification images of nanospheres and (c) nanorods. (d) HRTEM image of nanospheres.

was analyzed by AFM. The 3D AFM image in Figure 8d shows the growth of irregular granular crystallites onto a glass substrate at 300 °C. The average roughnesses of the films are 13 nm at 350 °C and 16 nm at 400 °C.

Conclusion

We have reported the synthesis, structures, and magnetic properties of some new iron(III) complexes of 1,1,5,5-tetra-alkyl-2-thiobiurets. The synthesis is straight from the reaction of diisopropylcarbamoyl chloride, sodium thiocyanate, and iron nitrate in the presence of dialkylamine, which produced new monomeric complexes; however, in the case of diethylamine, a methoxide-bridged binuclear iron(III) complex seems to predominate. Single-crystal X-ray structures of complexes **1**, **2**, and **4** all showed distorted octahedral geometries at the iron(III) ion. Magnetic measurement for complex **2** confirmed its antiferromagnetic behavior. TGA showed the single-step decomposition of complexes **1**, **3**, and **4** and the double-step decomposition for complex **2**. The newly synthesized complexes were used as single-source precursors for the deposition of iron sulfide thin films by AACVD. The relative stabilities of various phases of iron sulfide are shown in Figure 16 using a plot similar to that developed by Vaughan and Lennie.[1] The height of the pyramid on the negative *z* axis represents the free energy of formation of each phase. The solid line represents the thermodynamic stability and connects the stable phases FeS (troilite) and FeS_2 (pyrite).[1] In our CVD work, we have almost always only seen the two most stable phases, with the exception of Fe_7S_8 (pyrrhotites) at 300 °C from complex **1**. This may suggest a reaction leading to predominantly thermodynamic products; i.e., once the system is sufficiently sulfiding for FeS_2 to form, only this phase or its mixtures with FeS is seen from films deposited using precursors **1**−**3**. There are apparently two known exceptions[36,38] to this rule in the CVD of FeS_x along with Fe_7S_8 from complex **1** at 300 °C (Supporting Information).

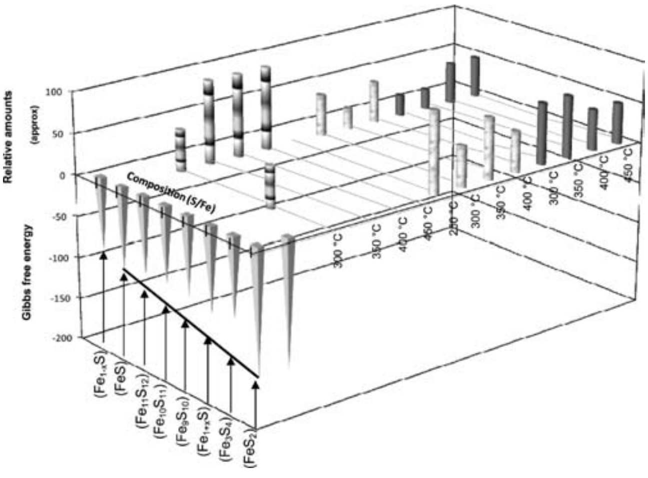

Figure 16. Phases of iron sulfide films deposited in CVD experiments from precursors **1**−**3**. The relative amount of each phase is represented as the height of the cylinder: small (25%), medium (50%), large (75%), and only one phase (100%). These are approximated based on the powder XRD results. Compared to the relative thermodynamic stabilities of the various phases of iron sulfides (the *z* axis) of the phases after Vaughan and Lennie.[1].

We can contrast this behavior with that observed in the deposition of FeS from solution, sometimes, as particles with critical dimensions on the order of nanometers. It is interesting that solution deposition, possibly because of the lower temperatures involved, can allow for the formation of less stable phases such as mackinawite, although the stoichiometry is controversial[1,3] $(Fe_{1+x}S)$,[13] pyrrhotite $(Fe_{1-x}S)$,[21,22,47] and greigite (Fe_3S_4)[14,18] which must form under kinetic control (Supporting Information). Indeed, there are many examples of such FeS phases in biology, notably in magnetotactic bacteria.[13,14,48,49]

Acknowledgment. K.R. is grateful to ORS and The University of Manchester for financial support. The authors also thank EPSRC, U.K., for grants to P.O.B. that made this research possible.

Supporting Information Available: XPS spectra, a TGA graph, magnetic measurements, an additional HRTEM image, a powder XRD pattern of films deposited from complex **3**, a graph showing a comparison of the Gibbs free energy with iron sulfide phases, and CIF files for compounds **1**, **2**, and **4**. This material is available free of charge via the Internet at http://pubs.acs.org.

---

(47) Lai, H. Y.; Chen, C. J. *J. Cryst. Growth* **2009**, *311*, 4698.
(48) Posfai, M.; Buseck, P. R.; Bazylinski, D. A.; Frankel, R. B. *Am. Mineral.* **1998**, *83*, 1469.
(49) Posfai, M.; Buseck, P. R.; Bazylinski, D. A.; Frankel, R. B. *Science* **1998**, *280*, 880.